





Inference of the force pattern acting on a semiflexible filament from shape analysisJulieta Wenger  and Azul Brigante *Universidad de Buenos Aires, Facultad de Ciencias Exactas y Naturales, Departamento de Física, C1428EGA Buenos Aires, Argentina*Agustina B. Fernández Casafuz  and Luciana Bruno *Universidad de Buenos Aires, Instituto de Cálculo (IC), C1428EGA Buenos Aires, Argentina
and Consejo Nacional de Investigaciones Científicas y Técnicas (CONICET), C1425FQD Buenos Aires, Argentina*Alejandro Monastera **Universidad Nacional de General Sarmiento, Instituto de Ciencias, B1613 Los Polvorines, Buenos Aires, Argentina
and Consejo Nacional de Investigaciones Científicas y Técnicas (CONICET), C1425FQD Buenos Aires, Argentina*

(Received 14 July 2023; accepted 6 November 2023; published 4 December 2023)

The study of the active forces acting on semiflexible filaments networks such as the cytoskeleton requires noninvasive tools able to explore the deformation of single filaments in their natural environment. We propose here a practical method based on the solution of the hydrodynamic beam equation in the presence of transverse forces. We found that the derivative of the local curvature presents discontinuities that match the location of the applied forces, in contrast to the smooth curvature function obtained for the case of compressing longitudinal forces. These patterns can be easily appreciated in a kymograph of the curvature, which also reflects the temporal behavior of the forces. We assessed the method performance with numerical simulations describing the deformation of single microtubules provoked by the action of intracellular active forces.

DOI: [10.1103/PhysRevE.108.064402](https://doi.org/10.1103/PhysRevE.108.064402)**I. INTRODUCTION**

Semiflexible filaments bend as the result of external forces acting over them. During the filament deformation, its shape changes are governed by the hydrodynamic beam equation [1]. However, inferring the forces involved in this process only by looking at the filament shape is not an easy task. This can be relevant in many practical applications. In particular, it is of interest when describing biological structures, such as cytoskeletal filaments and cellular cilia. In these examples, active forces are responsible for the dynamical deformations, and hence an analysis of the shape fluctuations of these filaments can reveal important aspects of the nature of the cytoplasmic environment [2].

In a seminal work, Gittes *et al.* [3] provided a methodology to solve the inverse problem for an isolated filament immersed in a fluid with known rheological properties, based on the theoretical formulation of Landau and Lifshitz [4]. They applied this method to estimate the force performed by a single kinesin motor when buckling a microtubule filament *in vitro*. A similar theoretical approach has been used to study microtubules in vesicles under tension to obtain the persistence length of microtubules [5]. These papers show that information on the forces deforming microtubules can be inferred from the inspection of their shapes under very well-controlled conditions. However, in living cells, microtubules are subject to stochastic forces, representing a challenge to

determine their spatiotemporal patterns by inspecting microtubules shapes.

Concerning this problem, Gladrow *et al.* [6] developed an analytical theory describing the shape fluctuations of an individual semiflexible probe filament in an active viscoelastic environment. The system is driven out of equilibrium by stochastic forces acting locally at fixed positions along the filament, which induce coupling between the flexural modes. These correlations give rise to effective circulatory currents in the mode's phase space that depend on the temporal behavior of motor activity. The authors propose that measuring cycling frequencies will be an ideal, noninvasive tool to detect and quantify motor activity in biological networks.

To test this approach, Battle *et al.* [7] have implemented the method proposed in [6] to study the force patterns operating on primary cilia and beating flagella. These two systems have the advantage that they present a periodic behavior sustained by molecular motors operating at one of their ends. This allows them to record the movement for several cycles and obtain long time series, providing data to build sufficiently populated phase diagrams in which the currents are evident. The authors were able to prove the nonequilibrium activity underlying the steady-state fluctuations in these two biological systems.

Despite the elegance of these recent works, their main drawback is that they require very long time series to allow a deep exploration of the phase space. Although this can be attainable for cyclical processes such as the beating of primary cilia, the sporadic bending and buckling of cytoskeletal filaments within cells cannot be attacked with

*amonastra@campus.ungs.edu.ar

those approaches. These frequent but stochastic events have gained interest recently due to their possible implications in mechanotransduction processes [8,9].

To address this problem, approaches based on numerical simulations of semiflexible filaments have been proposed [10–12], mostly orientated to the description of the nonequilibrium origin of the fluctuations. Experimental evidence of these nonthermal fluctuations has been observed for a microtubule immersed in an active actin gel [13]; assuming pointlike transverse forces acting on the filament and an elastic medium, the authors were able to estimate the magnitude of the active forces deforming the microtubule. In a more recent paper [14], fluorescent microtubules in *Xenopus laevis* melanophores were tracked and buckling events were characterized. These experimental observations were compared to numerical simulations of a discretized one-dimensional (1D) semiflexible filament immersed in a homogeneous medium, with a viscosity similar to that reported for the cell cytoplasm. External forces with different directions and magnitudes were also considered in the model, and the evolution of the filament shape was characterized. It was shown that different force scenarios could give rise to very similar deformations, making the characterization of forces very challenging in practice.

In an aim to overcome this difficulty, we propose here the basis of a method to infer the forces transiently deforming a semiflexible filament immersed in a viscous fluid from the inspection of spatiotemporal curvature intensity matrices, i.e., curvature kymographs. The method grounds in the solution of the hydrodynamic beam equation in the presence of transverse forces, where we found that the local curvature presents discontinuities that match the applied force patterns and that can be easily appreciated in a heat map of the curvature. We assessed the method performance with numerical simulations, considering different force scenarios, and its applicability to noisy data.

II. MECHANICAL MODEL

The configuration of the filament is defined by the position of its neutral axis $\mathbf{r}(s)$, with s a coordinate along the filament in the range $0 \leq s \leq L$, where L is the natural length of the filament. The coordinate s defines the material point, and the filament can undergo two types of deformation: strain $\varepsilon(s)$, given by local tension compression, and curvature $\mathcal{C}(s)$,

$$\varepsilon(s) = |\mathbf{r}'(s)| - 1, \quad (1)$$

$$\mathcal{C}(s) = \frac{|\mathbf{r}'(s) \times \mathbf{r}''(s)|}{|\mathbf{r}'(s)|^3}. \quad (2)$$

In the case of deformations in a plane, instead of using the Cartesian coordinates (x, y) of the material points, we can use the local strain $\varepsilon(s)$ and tangent angle $\theta(s)$ of the filament (with respect to the x axis), as the functions to characterize the filament shape; see Fig. 1.

Given these two functions, we can recover the Cartesian coordinates integrating

$$x(s) = x_0 + \int_{s_0}^s ds' [1 + \varepsilon(s')] \cos \theta(s'), \quad (3)$$

$$y(s) = y_0 + \int_{s_0}^s ds' [1 + \varepsilon(s')] \sin \theta(s'). \quad (4)$$

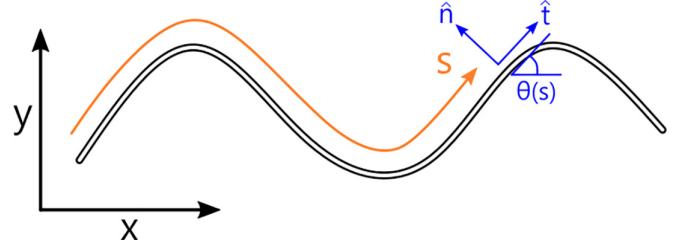


FIG. 1. An arbitrary configuration of the filament that can be described by Cartesian coordinates $x(s)$ and $y(s)$, or by the tangent angle $\theta(s)$, as a function of the material point coordinate s .

The material point s_0 is taken as an arbitrary origin, with Cartesian coordinates (x_0, y_0) . For most analysis, we choose $s_0 = 0$ at one end of the filament ($0 \leq s \leq L$). For analytical calculations, for symmetry reasons it is more practical to choose s_0 in the middle of the filament, so $-L/2 \leq s \leq L/2$.

Computing the first and second derivatives of expressions (3) and (4), it is easy to demonstrate that the curvature is

$$\mathcal{C}(s) = \frac{\theta'}{1 + \varepsilon}. \quad (5)$$

Elastic energy V_E due to pure tension or compression of the filament, and bending energy V_B , are given by

$$V_E = \frac{1}{2}EA \int_{-L/2}^{L/2} \varepsilon^2(s) ds, \quad (6)$$

$$V_B = \frac{1}{2}EI \int_{-L/2}^{L/2} [\theta'(s)]^2 ds, \quad (7)$$

where A and I are the cross-sectional area of the filament and the second moment of the area, respectively, and E is the Young's modulus of the material. The flexural rigidity of the filament is defined as EI .

Applying a variational principle to the elastic and bending energies, we obtain the corresponding forces,

$$\mathbf{f}_E = EA[\varepsilon' \hat{\mathbf{t}} + \varepsilon \theta' \hat{\mathbf{n}}], \quad (8)$$

$$\mathbf{f}_B = EI \left\{ \frac{\theta' \theta''}{1 + \varepsilon} \hat{\mathbf{t}} + \left[\frac{-3\varepsilon'' \theta' + \varepsilon' \theta''}{(1 + \varepsilon)^2} + \frac{3\theta'^3 - \theta'''}{1 + \varepsilon} \right] \hat{\mathbf{n}} \right\}, \quad (9)$$

where $\hat{\mathbf{n}}$ and $\hat{\mathbf{t}}$ are the normal and tangent local unit vectors to the filament; see Fig. 1.

We consider a viscous force $\mathbf{f}_V = -c\dot{\mathbf{r}}$ that depends on the velocity of the material point,

$$\dot{\mathbf{r}}(s, t) = \frac{d\mathbf{r}}{dt} = \dot{\mathbf{r}}_0 + \int_{s_0}^s ds' [\dot{\varepsilon} \hat{\mathbf{t}}(s') + (1 + \varepsilon) \dot{\theta} \hat{\mathbf{n}}(s')], \quad (10)$$

where $\dot{\varepsilon}$ and $\dot{\theta}$ are the partial derivatives with respect to time, and c is a drag coefficient per unit length. This coefficient is proportional to the dynamic viscosity of the fluid and depends on the shape of the transverse section.

Collecting all the forces and neglecting the inertia (overdamped regime), we obtain the hydrodynamic equation

$$\mathbf{f}_E + \mathbf{f}_B + \mathbf{f}_V + \mathbf{f}_{\text{ext}} = 0, \quad (11)$$

where \mathbf{f}_{ext} represents any external force applied to the filament. Equation (11) is a nonlinear integro-differential equation which determines the time evolution of strain $\varepsilon(s)$

and tangent angle $\theta(s)$ from an initial configuration, given the appropriate boundary conditions of the problem.

Due to the nonlinear terms in the forces, the evolution of the filament shape cannot be solved analytically. However, we can linearize the problem making some reasonable approximations. First, we consider that the strain along the filament is very small, $\varepsilon(s) \ll 1$ (inextensible filament). It will be shown later that for slender filaments, even in the case of important initial strain, the timescale in which it relaxes is much faster than the timescale for curvature relaxation. With this approximation, the curvature $\mathcal{C}(s)$ is practically identical to the first derivative of the tangent angle, $\theta'(s)$.

Second, we consider small curvatures, $|\mathcal{C}| \ll 1/L$. Moreover, to avoid the integral necessary to compute the velocity, we can derive the hydrodynamic Eq. (11) with respect to s , obtaining, up to first order,

$$\frac{\partial \mathbf{f}_E}{\partial s} = EA \varepsilon''(s) \hat{\mathbf{t}}, \quad (12)$$

$$\frac{\partial \mathbf{f}_B}{\partial s} = -EI \theta''''(s) \hat{\mathbf{n}}, \quad (13)$$

$$\frac{\partial \mathbf{f}_V}{\partial s} = -c[\dot{\varepsilon} \hat{\mathbf{t}} + \dot{\theta} \hat{\mathbf{n}}]. \quad (14)$$

Therefore, for a filament without external forces (or portions of the filament where no external forces are applied), we obtain two decoupled differential equations: one in the tangent direction, which provides the evolution of the strain, and the other in the normal direction, which provides the evolution of the curvature:

$$0 = EA \varepsilon'' - c \dot{\varepsilon}, \quad (15)$$

$$0 = -EI \theta'''' - c \dot{\theta}. \quad (16)$$

Equation (16) is analogous to the equation for the transverse displacement in a beam, as studied in [4].

For the condition of no tension at the filament ends, $\varepsilon(s = \pm L/2) = 0$, Eq. (15) can be easily solved, obtaining

$$\varepsilon(s, t) = \sum_{n=1} b_n \Phi_n(s) \exp(-n^2 t / \tau_E), \quad (17)$$

with Fourier modes

$$\Phi_n(s) = \frac{1}{\sqrt{L}} \cos(n\pi s/L), \quad n \text{ odd}, \quad (18)$$

$$\Phi_n(s) = \frac{1}{\sqrt{L}} \sin(n\pi s/L), \quad n \text{ even}, \quad (19)$$

and

$$\tau_E = \frac{cL^2}{\pi^2 EA} \quad (20)$$

is the characteristic *elastic* time.

For the tangent angle evolution, the solution of the differential Eq. (16) for a free filament, imposing no curvature at the filament ends $\mathcal{C}(s = \pm L/2) = 0$, gives the normal modes:

$$\Psi_n(s) = \frac{\sqrt{L}}{\kappa_n} \left[\frac{\sinh(\kappa_n s/L)}{\cosh(\kappa_n/2)} - \frac{\sin(\kappa_n s/L)}{\cos(\kappa_n/2)} \right], \quad n \text{ odd}, \quad (21)$$

$$\Psi_n(s) = \frac{\sqrt{L}}{\kappa_n} \left[\frac{\cosh(\kappa_n s/L)}{\sinh(\kappa_n/2)} + \frac{\cos(\kappa_n s/L)}{\sin(\kappa_n/2)} \right], \quad n \text{ even}, \quad (22)$$

with $\kappa_1 = 4.73004$, $\kappa_2 = 7.8532$, and $\kappa_n \approx \pi(n + 1/2)$. The derivative with respect to s of these modes (curvature modes) fulfills the orthonormal condition

$$\int_{-L/2}^{L/2} ds \Psi'_n(s) \Psi'_m(s) = \delta_{nm}. \quad (23)$$

We remark that for different boundary conditions, other modes with a similar functional behavior, but different wave numbers, can be obtained. Finally, the general solution for the tangent angle of a free filament is

$$\theta(s, t) = \theta_0 + \sum_{n=1} a_n \Psi_n(s) \exp(-\Gamma_n t). \quad (24)$$

The coefficients are obtained from the curvature of the filament using the orthonormal condition

$$a_n = \int_{-L/2}^{L/2} ds \Psi'_n(s) \theta'(s). \quad (25)$$

Each mode has its characteristic damping rate,

$$\Gamma_n = \frac{EI \kappa_n^4}{cL^4}. \quad (26)$$

This gives the longest timescale for the relaxation of the first mode,

$$\tau_B = \frac{cL^4}{EI \kappa_1^4}, \quad (27)$$

that we call *bending* time. For a slender filament where $L \gg \phi$, and ϕ is its diameter, this timescale is approximately $(L/\phi)^2$ times larger than the elastic time computed before. Therefore, for the purpose of this work, besides considering that the strain is very small, it evolves *instantly* compared to the evolution of the curvature.

A. Localized transverse forces

The differential equation (16) also has a cubic polynomial as a stationary solution ($t \rightarrow \infty$), valid for portions of the filament where the external force is zero.

Now, we consider the presence of external forces in the perpendicular direction to the filament. From the most general case of a continuous distribution, $\mathbf{f}_{\text{ext}}(s) = f(s) \hat{\mathbf{n}}$, we concentrate on the limit of a punctual force $\mathbf{f}_{\text{ext}}(s) = F \delta(s - s_i) \hat{\mathbf{n}}$. Here, s_i is the coordinate of the material point on the filament where this punctual external force is applied. The sign of F is positive when it is parallel to $\hat{\mathbf{n}}$, and negative otherwise.

Integrating Eq. (11) gives a condition for the tangent angle [4],

$$-EI\theta''(s_i^-) = -EI\theta''(s_i^+) + F, \quad (28)$$

resulting in a discontinuity for the second derivative of the tangent angle at the point where the force is applied. This condition is independent of the rheological properties of the medium and is analogous to the discontinuity of the third derivative of the displacement in the beam equation, given by a punctual shear [4].

Taking into account this condition, and that for a free filament the curvature is zero at the ends, the stationary solution

is the polynomial,

$$\begin{aligned} \Theta(s_i, F, s) = & \frac{FL^2}{EI} \left[-\frac{\sigma_i}{2} \left(\frac{s}{L}\right)^4 - \frac{1}{6} \left(\frac{s}{L}\right)^3 \right. \\ & + \frac{3\sigma_i + \text{sign}(s - s_i)}{4} \left(\frac{s}{L}\right)^2 \\ & - \frac{4\sigma_i \text{sign}(s - s_i) + 1}{8} \left(\frac{s}{L}\right) \\ & \left. + \frac{\text{sign}(s_i) + \text{sign}(s - s_i)}{4} \sigma_i^2 \right] + \omega t, \quad (29) \end{aligned}$$

where $\sigma_i = s_i/L$ and $\omega = 12\sigma_i F/(cL^2)$. Therefore, by only giving the value of the force F and its position s_i on the filament, we can build the solution for $\theta(s)$ that gives the stationary shape of the filament for $t \rightarrow \infty$. Due to the external force and torque, the filament could have a global velocity and rotation. However, this is irrelevant if we are only interested in its shape.

In the presence of several external localized forces, the stationary solution is given by the superposition of solutions (29),

$$\Theta_\infty(s) = \theta_0 + \sum_i \Theta(s_i, F_i, s). \quad (30)$$

We expect that for any arbitrary initial deformation of the filament, if the position and value of the applied external forces remain constant in time, for $t \gg \tau_B$ the shape of the filament will tend to $\Theta_\infty(s)$. We can consider this shape as an *attractor* in the space of configurations, given the external force pattern.

For the transient regime, we should go back to the previous solutions in terms of flexural modes. Given an initial configuration of the filament $\Theta_0(s)$ at time $t = 0$, we can write it as

$$\theta(s, t = 0) = \Theta_0(s) = \Theta_0(s) - \Theta_\infty(s) + \Theta_\infty(s). \quad (31)$$

Knowing the stationary solution, we expect that the first two terms $\Theta_0(s) - \Theta_\infty(s)$ should decay in time. So we can expand them in flexural modes,

$$\theta(s, t) = \theta_0 - \Phi + \sum_{n=1} a_n \Psi_n(s) \exp(-\Gamma_n t) + \Theta_\infty(s) \quad (32)$$

with

$$a_n = \int_{-L/2}^{L/2} ds \Psi'_n(s) [\Theta'_0(s) - \Theta'_\infty(s)], \quad (33)$$

$$\Phi \equiv \sum_{m=1} a_{2m} \Psi_{2m}(0). \quad (34)$$

Considering stochastic forces that turn *on* and *off* in time, each time that there is a change of them, the new asymptotic solution has to be computed and the decomposition in modes of the instantaneous configuration should be done again.

These results suggest that the analysis of the curvature would be a good indicator of spatial location and temporal dynamics of the forces acting on the filament. We will explore the scope of this approach using numerical simulations later in this work.

TABLE I. Parameters used in the simulations.

| | | |
|--------------------------------|--|--------------|
| Filament length (L) | 10 μm | |
| Filament diameter (ϕ) | 25 nm | Ref. [1] |
| Flexural rigidity (EI) | 2×10^7 pN nm ² | Ref. [18] |
| Elastic constant (EA) | 10^4 pN | Ref. [1] |
| Drag coefficient (c_\perp) | 1.84×10^{-5} pN s/nm ² | Ref. [14] |
| Viscosity (η) | 10^{-5} pN s/nm ² | Ref. [14] |
| Thermal energy ($k_B T$) | 4 pN nm | |
| Active forces (f) | 50–200 pN | Refs. [3,14] |

B. Compressing forces

Compressing longitudinal forces applied to a filament can trigger a buckling event resulting in its bending. This phenomenon is a consequence of the instability produced along the filament shape when the magnitude of the applied force overcomes a critical value. This critical force or Euler force depends on the length L and flexural rigidity EI , and is defined as [1,4]

$$F_c = \alpha \frac{EI}{L^2}, \quad (35)$$

with α a constant that depends on the boundary conditions.

In this scenario, the solution of the curvature equation results in normal modes that are different from the ones obtained for transverse forces. The major change is that some modes have a positive growing rate in time [15], if the compressing force is larger than F_c . Due to the unstable nature of the buckling process, minuscule curvatures on the initial filament's configuration can grow fast to large values.

If the compressing force largely exceeds its critical value, high wave numbers are expected, and several points with large positive and negative curvature alternate along the filament shape. However, the growing normal modes during the buckling process do not show discontinuities in the curvature or its derivative, which is a key difference with the case of transverse forces.

III. NUMERICAL SIMULATIONS

In the previous section, we obtained analytical expressions for the evolution of the shape of a filament immersed in a viscous medium in the presence of transverse or longitudinal forces. However, when several forces with stochastic behaviors in space and time act on the filament, the complexity to predict the filament shape evolution increases. As also mentioned, in the case of forces with a parallel component to the filament, the buckling phenomenon can arise, which is very sensitive to the initial conditions [15], making the exact moment of the onset of the bending process analytically unpredictable.

Therefore, to study these scenarios, we performed numerical simulations of a single filament using the wormlike chain model [16], such as described in [14,15,17] (for details, see the Appendix).

We run simulations of this model using the parameters displayed in Table I, which correspond to a microtubule immersed in a medium with a viscosity resembling that of the cytoplasm. These physical parameters give an elastic time

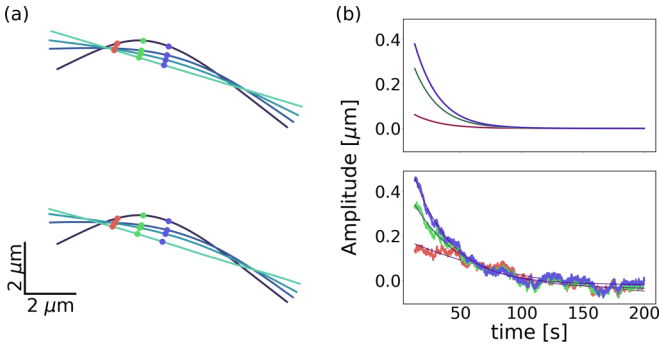


FIG. 2. Simulation of a 10 μm microtubule in a viscous medium, during a relaxation without external forces, with and without thermal agitation. The filament was initially bent. (a) Simulated shapes for increasing times (from dark to light blue), without (with) thermal agitation in the upper (lower) panel. (b) Amplitude of the colored beads marked in (a), computed as the distance to their final position. The amplitudes of individual beads show slight variations due to thermal noise [lower vs upper panel in (b)], although their shapes and characteristic relaxation times are very similar.

$\tau_E = 0.0186\text{ s}$ and bending time $\tau_B = 18.4\text{ s}$. This difference in the timescale of both processes is consistent with our assumption of a slender filament.

In the simulations, the filament is discretized by dividing it into $N = 100$ segments of equal length, $\Delta s = 100\text{ nm}$. The integration temporal step was $\Delta t = 5\ \mu\text{s}$.

We should mention that due to the high stiffness of microtubules, which results in a persistence length $L_p = EI/(k_B T) \approx 5\text{ mm}$ [18,19], much larger than the typical length of microtubules in their natural environment, thermal forces do not significantly affect the filament's shapes (Fig. 2). Thus, we did not consider thermal noise in what follows.

Similarly to [6], localized active forces f applied at discrete positions along the filament with a stochastic temporal behavior were considered. The temporal pattern followed a telegraph function with a characteristic times τ_{ON} and τ_{OFF} . We also explored the effects of longitudinal stochastic forces applied at one or both filament ends.

The obtained discrete $[x(t), y(t)]$ coordinates of the filament shape for each time t were transformed into the discrete curvilinear coordinates, $\theta(s)$, for the tangent angle of each segment. The curvature was obtained as the discrete centered derivative of $\theta(s)$.

In order to facilitate the visualization of the filament shape evolution in time, we introduce a graphical tool: the kymograph of curvature. This colored image is built as a matrix whose rows and columns represent the curvature along s and time, respectively, while the color intensity value represents the curvature magnitude. The inspection of these matrices allows the visualization of the spatiotemporal force patterns, as will be discussed in the following sections.

A. Curvature analysis for transverse and longitudinal forces

We first consider the case of a single force $F = 50\text{ pN}$, acting perpendicularly on a $10\ \mu\text{m}$ filament at the position $s_i = 3.3\ \mu\text{m}$. The dependence in time is a telegraph function: if the force is off, it activates with a Poissonian probability with

characteristic time $\tau_{\text{ON}} = 3\text{ s}$; while if the force is on, it deactivates with a Poissonian probability with time $\tau_{\text{OFF}} = 1.3\text{ s}$.

The left panel of Fig. 3(a) shows the configuration of the filament at two different times: one when the force is on, the other when the force is off. The corresponding curvature profiles along the filament are plotted in the left panel of Fig. 3(b). When the force is on, the pointy shape displayed by the curvature at the position $s = 3.3\ \mu\text{m}$ is noticeable, which corresponds to the point of application of the force s_i . This is a manifestation of the discontinuity of the curvature derivative at s_i .

In the left panel of Fig. 3(c), we show the curvature of the filament as a function of time at $s = 3.3\ \mu\text{m}$ and $s = 6.7\ \mu\text{m}$. For the first position, a rapid increase in the curvature magnitude is observed when the force switches from off to on. The release of the force triggers the rapid decrease of the curvature, which corresponds to the relaxation of the filament shape. Although the amplitudes are smaller, the other temporal profile displays a similar behavior. The exponential decay of the curvature when the force is off is in agreement with the characteristic bending time, $\tau_B = 18.4\text{ s}$, as expected since the relaxation rate only depends on the geometrical and mechanical properties of the filament and the medium viscosity.

Finally, in the left panel of Fig. 3(d), we present a kymograph that displays the curvature values both as a function of position s along the filament (horizontal axis) and time (vertical axis). The horizontal colored lines in the kymograph indicate the two instants studied in Fig. 3(b), while the vertical colored lines correspond to the positions analyzed in Fig. 3(c). The position where the force is applied can be inferred from the inspection of the curvature around the extreme values in the kymograph. Additionally, the temporal behavior of the force can be explored by counting the spots along the vertical line at this maxima position.

We now consider the case of a 50 pN compressing force acting on the right end of the filament, while the left end is fixed. The time dependence is also chosen as a telegraph function with the same τ_{ON} and τ_{OFF} as the previous case. The angle of the force is chosen randomly between $\pm 30^\circ$ in each activation event, so its main component is in the compressing direction. The modulus is larger than the Euler's critical load, which for this case is near 2 pN , provoking a buckling instability. In the right panel of Fig. 3(a), we represent two configurations of the filament, with the force on and off, respectively. The characteristic wavy shapes are similar to the case of the transverse force discussed above, and it is almost impossible to infer the nature of the force acting on the filament only by looking at the shapes. However, in the right panel of Fig. 3(b), we observe a striking difference in the curvature profile compared to its counterpart for the transverse force. The curvature is bell shaped and does not show any cusp or discontinuity in its derivative, even when the force is on.

On the other hand, the temporal behavior of the bending and relaxation processes produced by the stochastic compressing force pattern is very similar to the one observed in the case of the transverse forces [Fig. 3(c)], also recovering the same relaxation times, as expected.

Finally, the kymograph for this case [right panel of Fig. 3(d)] displays a similar pattern as in the case of the

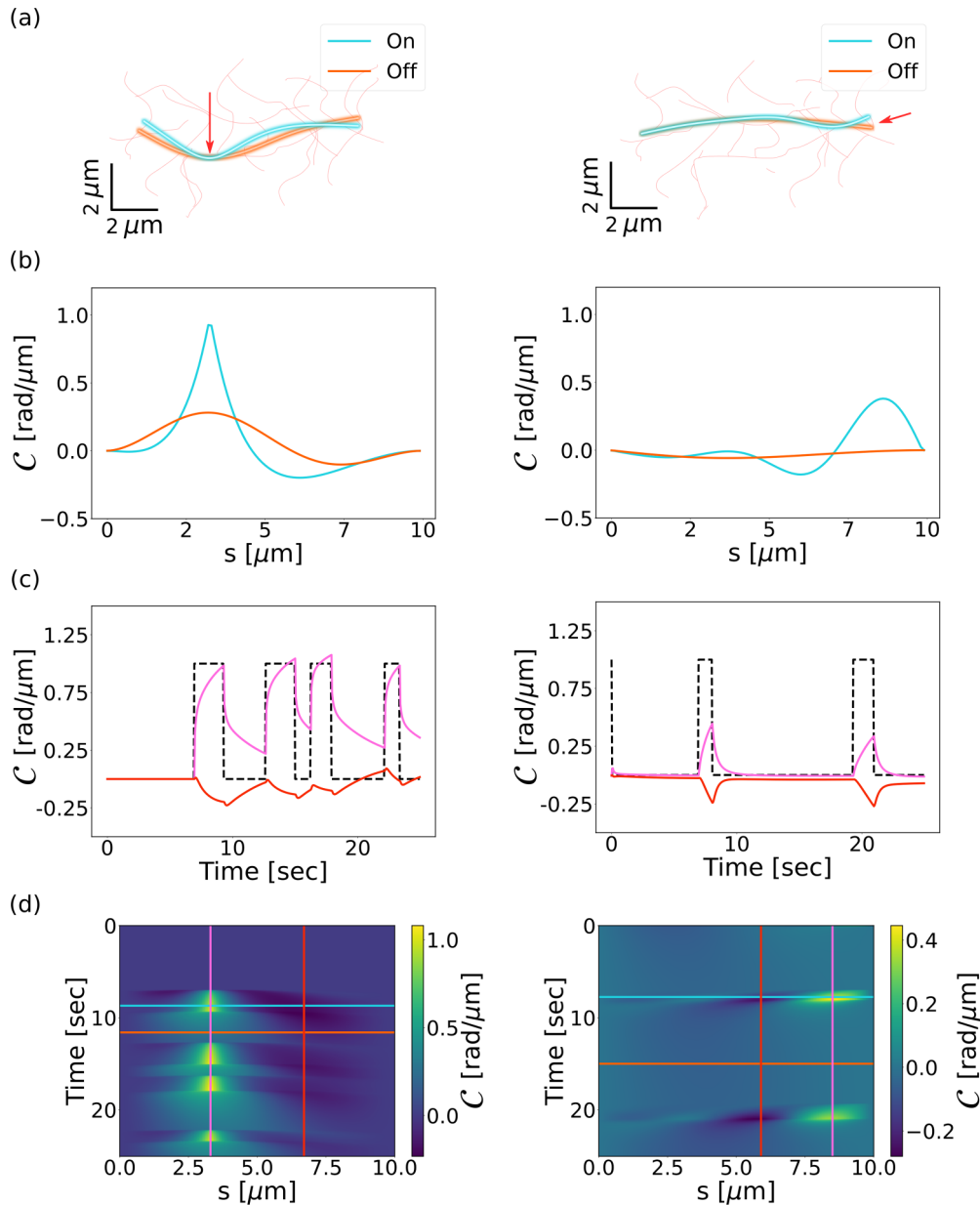


FIG. 3. Comparison between the action of a 50 pN transverse force (left panels) and a 50 pN longitudinal compressing force (right panels). (a) Configuration of the microtubule at two different times, when the force is on (blue) and off (orange). The red arrows indicate the position and direction of the forces. (b) Curvature as a function of the coordinate s along the filament, with the same instants and color code as (a). (c) Curvature as a function of time at two different positions (magenta and red lines). The dashed line represents the force temporal on and off behavior (in arbitrary units). (d) Curvature spatiotemporal kymographs. Horizontal colored lines at different times for the configuration and curvature profiles represented in (a) and (b). Vertical colored lines show the positions of the temporal profiles shown in (c).

transverse force. However, the localization of the extreme values of the curvature slightly varies, which is a typical feature of the buckling process evolution.

To sum up, while the curvature vs s profile allows exploring the spatial localization and direction of the forces acting on the filament, the curvature vs t plot gives an insight into the temporal dynamics of the applied forces. In addition, the exploration of the curvature during the relaxation periods provides information about the mechanical properties of the filament and the viscosity of the environment.

B. Inferring the spatiotemporal force patterns from the curvature's kymograph

We consider here two different scenarios. In the first place, we simulate the action of intermittent and transverse forces acting at six different positions along a filament, as represented in Fig. 4(a). In this case, the kymograph is more complex than the one shown in Fig. 3. However, the points of application of the forces can be appreciated, corresponding to areas of intense yellow (for positive curvatures) and intense blue (for negative curvatures). Then, it is possible to choose

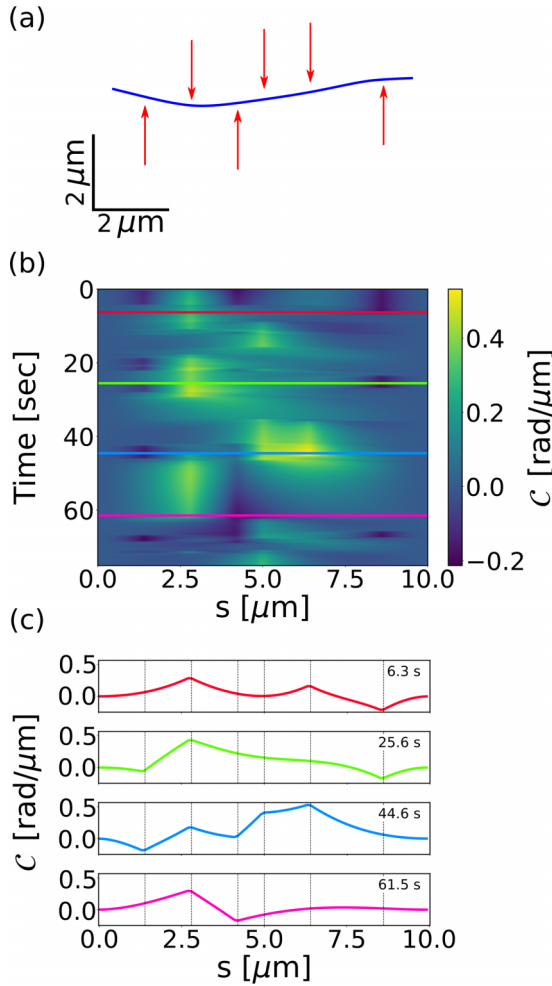


FIG. 4. Filament subject to the action of several stochastic forces. (a) Six transverse forces were applied at the points indicated by the red arrows, with the same simulation parameters as in Fig. 3. (b) Curvature kymograph displaying intense yellow and blue at the points of the force application. (c) Curvature profiles at different times, as indicated by the color lines in (b). These curves are not derivable when the forces are on at the point of their application (i.e., pointy shape).

some spatial profiles [indicated by the colored lines in the example shown in Fig. 4(b)] of curvature as a function of s and explore their behavior. Following the lesson learned for the case of a single transverse force, the extreme values of $\mathcal{C}(s)$ are candidates for points of force localization, as long as the curvature is not differentiable. A systematic exploration of those chosen spatial profiles can reveal not only the presence of local forces, but also their localization, as schematized in Fig. 4(c).

In the second case, we analyzed the buckling event produced by a large and almost instantaneous longitudinal force applied at one of the filament’s ends [Fig. 5(a)]. In this case, the instability gives rise to a multimodal deformation of the filament, as explored in [15,17]. At first sight, the resulting kymograph also shows regions of large positive and negative curvature [Fig. 5(b)]. However, a closer inspection reveals two interesting aspects: a temporal drift of the position of these

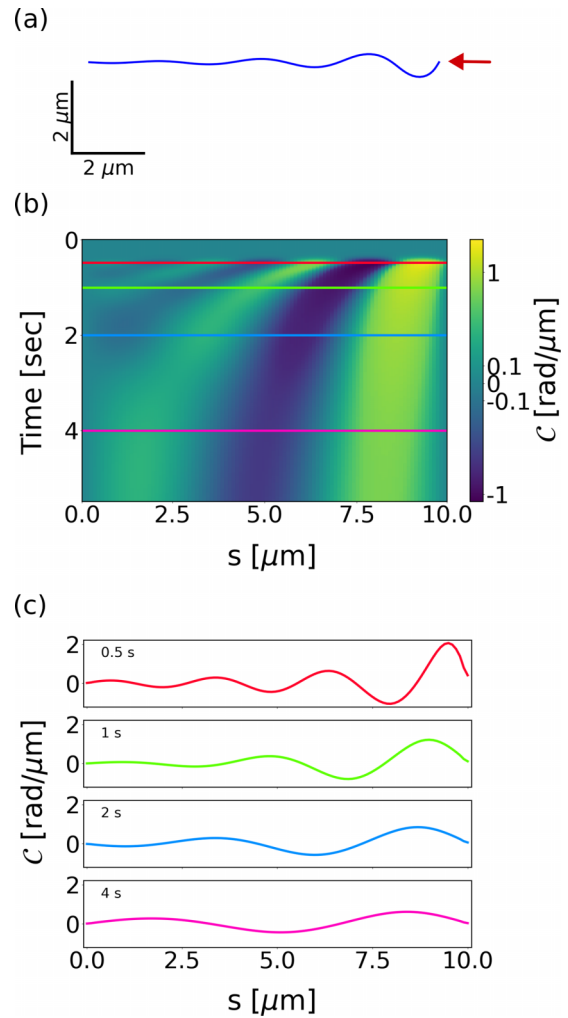


FIG. 5. Buckling of the filament by application of a large longitudinal force. (a) A 200 pN force was applied to one end of the filament (red arrow) at $t = 0$ s for approximately 0.5 s, resulting in its deformation. (b) Curvature kymograph displaying a multimodal behavior. (c) Curvature profiles at different times are indicated by the color lines in (b). These curves are derivable at every point for any time that is given (i.e., bell shape).

maxima and the absence of discontinuities of \mathcal{C}' , as evidenced in Fig. 5(c). These two aspects rule out the possibility that the forces responsible for the deformations are applied at positions $0 < s < L$.

C. Noisy data

The calculation of the curvature of real filaments can result in noisy data since it involves derivatives of the tangent angle obtained from discrete data points subject to the finite precision of the tracking method. In order to assess the impact of the tracking error on microtubule shape recovery, we simulated the behavior of a filament in a viscous medium under the influence of an intermittent transverse force of 50 pN applied at one-third of the filament length. The force is on from $t = 5$ to 8 s and from $t = 15$ to 17 s. For the rest of the simulation, the force is off. We assigned a random displacement sampled from a normal distribution with a standard deviation of 5 nm

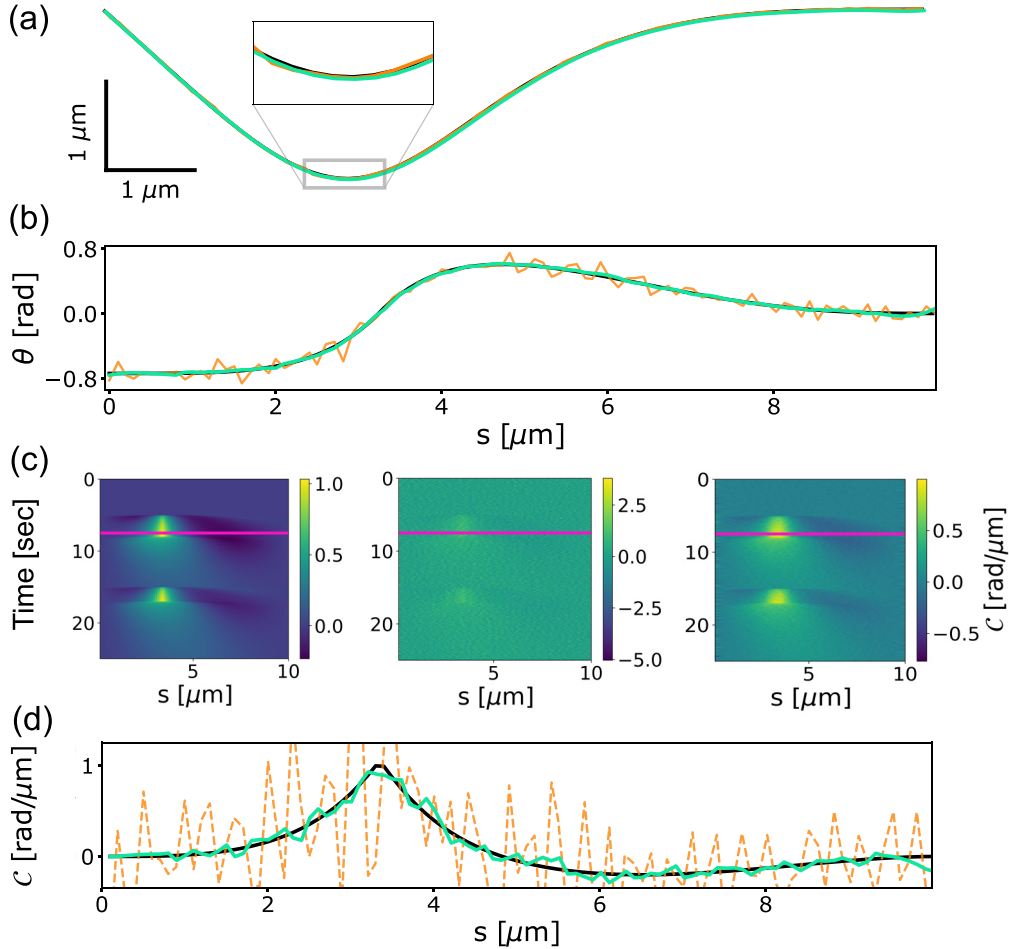


FIG. 6. Comparison between original, noisy, and smoothed simulated filaments subjected to intermittent forces. (a) Original (black), noisy (orange), and smoothed (green) filament shape at time $t = 7.5$ s. (b) Tangent angle $\theta(s)$ corresponding to the configuration shown in (a). (c) Curvature kymograph without error (left), with error (center), and with error and smoothing (right). The magenta line indicates the cut on the kymograph at time $t = 7.5$ s. (d) Curvature at time $t = 7.5$ s; same color code as specified in (a).

to the y position of each bead in the original simulation. This quantity corresponds to the typical precision achieved by filament tracking algorithms for high signal-to-noise ratio images [20], such as the ones obtained with Airyscan microscopy.

Figure 6 shows that the tracking error introduces small random fluctuations to the filament shape, that are amplified in the calculation of $\theta(s)$ and C . In order to analyze whether the application of a smoothing technique would enable the recovery of the curvature with higher precision, we tried the Savitzky-Golay filter available on PYTHON [21]. We decided to apply this filter to the noisy $\theta(s)$ data instead of the (x, y) coordinates because typical smoothing filters require 1D functions. Then, we recovered $C(s)$ deriving the smoothed $\theta(s)$ function. Transforming the θ and s coordinates back to the Cartesian ones using Eqs. (3) and (4) allowed us to reconstruct the smoothed filament shape.

Figure 6 shows the comparison between the original, the noisy, and the smoothed filament shape [Fig. 6(a)] and tangent angle [Fig. 6(b)] obtained in a simulation, with the same parameters as in Fig. 3. Although the shapes are very similar, the tracking error deeply impacts the calculation of the curvature, resulting in very noisy kymographs [Fig. 6(c)], which

completely shields the presence of the discontinuity. On the contrary, the smoothing procedure allows recovering the main features of the spatiotemporal force patterns observed in the original data [Fig. 6(d)].

IV. CONCLUSIONS

The study of the dynamics of cytoskeletal networks requires the search for noninvasive tools able to explore the deformation of single filaments in their natural environment. Fluorescence microscopy and tracking algorithms are well-known techniques to perform these studies [3,10,14]. However, inferring the forces responsible for the observed filament shapes is not straightforward.

Previous works, both by other researchers [5,18,22–24] and ourselves [14,17], have exhaustively analyzed the microtubule buckling phenomenon, which results from an instability in semiflexible filaments when subjected to compressing forces exceeding the critical force. It commonly occurs within cells, such as during microtubule polymerization when encountering obstacles or due to the push or pull of molecular motors. Conversely, the impact of transverse

forces on filament shapes has received significantly less attention in the biological context. Through numerical simulations presented in [14], we have demonstrated that the shapes of filaments subjected to transverse forces closely resemble those produced by compressing ones, despite significant differences in force intensity between the two cases. Therefore, the development of a method enabling the recovery of the points of force application would enhance our ability to determine their magnitudes accurately, which is crucial for understanding cellular mechanics. Although other approaches have been proposed [6,7], these methods require a stationary force pattern, where forces are always applied at the same spots along the filament, which makes them fail in cases of short time series and/or aleatory forces.

In this paper, we have applied a theoretical model of the local curvature of a semiflexible filament subjected to transverse or longitudinal forces. We found that the kymograph of the curvature reflects the underlying spatiotemporal force patterns. Closer inspection of the curvature \mathcal{C} vs s profiles at their extreme values allows distinguishing between localized transverse forces (pointy shape) and longitudinal forces (bell shape), even when this difference is not appreciable at first glance from the shape of the filament. At the same time, the curvature \mathcal{C} vs t profiles reveal the temporal activation and deactivation behavior of the applied forces.

In contrast to the mentioned works, our approach is also applicable to cases of sporadic deformations, such as microtubule bending, and short time series, which represents an advantage from an experimental point of view.

In the presence of noisy data, such as the discrete shapes recovered from the images of experimental filaments with a tracking algorithm, we demonstrated that the key features of the force pattern can be recovered after applying a standard smoothing procedure for the shapes.

Although the method was tested with numerical simulations of microtubules, these results can be extended to other cytoskeletal filaments, as well as semiflexible micro- and macroscopic fibers.

ACKNOWLEDGMENTS

This research was supported by Agencia Nacional de Promoción Científica y Tecnológica, Argentina (Grant No. PICT 2019- 2185). L.B. and A.G.M. are members of CONICET.

APPENDIX: NUMERICAL SIMULATIONS

We consider the wormlike chain model, as was described in [15]. We divide the filament in N equal segments of length

$\Delta s = L/N$. The configuration is determined by the $(N + 1)$ coordinates \mathbf{r}_n of the endpoints of each segment, where $0 \leq n \leq N$. In terms of these coordinates, the elastic and bending potential energies are written as

$$V_E = \frac{1}{2} \frac{EA}{\Delta l} \sum_{n=0}^{N-1} (|\mathbf{r}_{n+1} - \mathbf{r}_n| - \Delta l)^2, \quad (\text{A1})$$

$$V_B = \frac{EI}{\Delta l} \sum_{n=1}^{N-1} \left[1 - \frac{(\mathbf{r}_{n+1} - \mathbf{r}_n) \cdot (\mathbf{r}_n - \mathbf{r}_{n-1})}{|\mathbf{r}_{n+1} - \mathbf{r}_n| |\mathbf{r}_n - \mathbf{r}_{n-1}|} \right]. \quad (\text{A2})$$

Other expressions can be considered, depending on how the discrete derivatives are defined, although these expressions converge to Eqs. (6) and (7) in the limit $\Delta l \rightarrow 0$. Deriving the potential energies with respect to the coordinate \mathbf{r}_n , elastic and bending forces are obtained,

$$\mathbf{F}_n^E = -\frac{\partial V_E}{\partial \mathbf{r}_n}, \quad (\text{A3})$$

$$\mathbf{F}_n^B = -\frac{\partial V_B}{\partial \mathbf{r}_n}, \quad (\text{A4})$$

which are applied to the corresponding bead n . The viscous force is given by $\mathbf{F}_n^{\text{vis}} = -c\Delta l \dot{\mathbf{r}}_n$ for $1 \leq n \leq (N - 1)$. For the end beads $n = 0$ and $n = N$, the viscous force is $\mathbf{F}_n^{\text{vis}} = -c(\Delta l/2)\dot{\mathbf{r}}_n$, corresponding to the drag on both ending semisegments.

Neglecting the inertia of the filament, we arrive at $(N + 1)$ coupled first-order differential equations,

$$\dot{\mathbf{r}}_n = \frac{\alpha_n}{c\Delta l} (\mathbf{F}_n^E + \mathbf{F}_n^B + \mathbf{F}_n^{\text{ext}}), \quad (\text{A5})$$

where $\alpha_n = 1$ for $1 \leq n \leq (N - 1)$, and $\alpha_n = 2$ for $n = 0$ and $n = N$. For microtubules, we chose the parameters E , A , I , and c in Table I. These equations are integrated numerically from a given initial configuration.

In the simulations where thermal noise was considered, an additional random displacement was added to the position of each bead,

$$\mathbf{r}_n = \frac{\alpha_n}{c} (\mathbf{F}_n^{\text{tot}}) \Delta t + \sqrt{\frac{2k_B T}{c}} \mathbf{w}_n \sqrt{\Delta t}, \quad (\text{A6})$$

with k_B the Boltzmann constant and T the absolute temperature. \mathbf{w}_n represents a vector of Gaussian random numbers with zero mean and unit variance [25].

[1] J. Howard *et al.*, *Mechanics of Motor Proteins and the Cytoskeleton* (Sinauer Associates, Sunderland, MA, 2001).
 [2] C. P. Brangwynne, G. H. Koenderink, F. C. MacKintosh, and D. A. Weitz, Cytoplasmic diffusion: Molecular motors mix it up, *J. Cell Biol.* **183**, 583 (2008).
 [3] F. Gittes, E. Meyhöfer, S. Baek, and J. Howard, Directional loading of the kinesin motor molecule as it buckles a microtubule, *Biophys. J.* **70**, 418 (1996).

[4] L. D. Landau and Y. M. Lifshitz, *Theory of Elasticity* (Pergamon Press, Oxford, UK, 1970).
 [5] M. Elbaum, D. Kuchnir Fygenon, and A. Libchaber, Buckling microtubules in vesicles, *Phys. Rev. Lett.* **76**, 4078 (1996).
 [6] J. Gladrow, N. Fakhri, F. C. MacKintosh, C. F. Schmidt, and C. P. Brodersz, Broken detailed balance of filament dynamics in active networks, *Phys. Rev. Lett.* **116**, 248301 (2016).

- [7] C. Battle, C. P. Broedersz, N. Fakhri, V. F. Geyer, J. Howard, C. F. Schmidt, and F. C. MacKintosh, Broken detailed balance at mesoscopic scales in active biological systems, *Science* **352**, 604 (2016).
- [8] N. Wang, Review of cellular mechanotransduction, *J. Phys. D* **50**, 233002 (2017).
- [9] A. R. Harris, P. Jreij, and D. A. Fletcher, Mechanotransduction by the actin cytoskeleton: Converting mechanical stimuli into biochemical signals, *Annu. Rev. Biophys.* **47**, 617 (2018).
- [10] C. P. Brangwynne, F. MacKintosh, and D. A. Weitz, Force fluctuations and polymerization dynamics of intracellular microtubules, *Proc. Natl. Acad. Sci.* **104**, 16128 (2007).
- [11] I. A. Kent, P. S. Rane, R. B. Dickinson, A. J. Ladd, and T. P. Lele, Transient pinning and pulling: a mechanism for bending microtubules, *PLoS ONE* **11**, e0151322 (2016).
- [12] I. Weber, C. Appert-Rolland, G. Schehr, and L. Santen, Nonequilibrium fluctuations of a semi-flexible filament driven by active cross-linkers, *Europhys. Lett.* **120**, 38006 (2018).
- [13] C. P. Brangwynne, G. H. Koenderink, F. C. MacKintosh, and D. A. Weitz, Nonequilibrium microtubule fluctuations in a model cytoskeleton, *Phys. Rev. Lett.* **100**, 118104 (2008).
- [14] C. Pallavicini, A. Monastra, N. Bardeci, D. Wetzler, V. Levi, and L. Bruno, Characterization of microtubule buckling in living cells, *Eur. Biophys. J.* **46**, 581 (2017).
- [15] A. G. Monastra, M. F. Carusela, M. V. D'Angelo, and L. Bruno, Filament instability under constant loads, *J. Phys.: Conf. Ser.* **1012**, 012010 (2018).
- [16] E. Gauger and H. Stark, Numerical study of a microscopic artificial swimmer, *Phys. Rev. E* **74**, 021907 (2006).
- [17] A. G. Monastra, M. F. Carusela, G. van der Velde, M. V. D'Angelo, and L. Bruno, Evolution of instabilities in filament buckling processes, *Phys. Rev. E* **99**, 033004 (2019).
- [18] F. Gittes, B. Mickey, J. Nettleton, and J. Howard, Flexural rigidity of microtubules and actin filaments measured from thermal fluctuations in shape, *J. Cell Biol.* **120**, 923 (1993).
- [19] F. Pampaloni, G. Lattanzi, A. Jonáš, T. Surrey, E. Frey, and E.-L. Florin, Thermal fluctuations of grafted microtubules provide evidence of a length-dependent persistence length, *Proc. Natl. Acad. Sci.* **103**, 10248 (2006).
- [20] C. Pallavicini, V. Levi, D. E. Wetzler, J. F. Angiolini, L. Benseñor, M. A. Despósito, and L. Bruno, Lateral motion and bending of microtubules studied with a new single-filament tracking routine in living cells, *Biophys. J.* **106**, 2625 (2014).
- [21] `savgol_filter`, https://docs.scipy.org/doc/scipy/reference/generated/scipy.signal.savgol_filter.html.
- [22] C. P. Brangwynne, F. C. MacKintosh, S. Kumar, N. A. Geisse, J. Talbot, L. Mahadevan, K. K. Parker, D. E. Ingber, and D. A. Weitz, Microtubules can bear enhanced compressive loads in living cells because of lateral reinforcement, *J. Cell Biol.* **173**, 733 (2006).
- [23] T. Li, A mechanics model of microtubule buckling in living cells, *J. Biomech.* **41**, 1722 (2008).
- [24] I. M. Kulić, A. E. Brown, H. Kim, C. Kural, B. Blehm, P. R. Selvin, P. C. Nelson, and V. I. Gelfand, The role of microtubule movement in bidirectional organelle transport, *Proc. Natl. Acad. Sci.* **105**, 10011 (2008).
- [25] G. Volpe and G. Volpe, Simulation of a Brownian particle in an optical trap, *Am. J. Phys.* **81**, 224 (2013).